

A Broadband Algorithm for Adiabatic Mode Evolution and An Application on Polarization Splitter-Rotator on LNOI Platform

Geng Chen^{a†}, Chijun Li^{a†}, Xuanhao Wang^a, Yuankang Huang^a, Siyu Lu^a, Yiqi Dai^a, Xiangyu Meng^a, Cheng Zeng^{a*} and Jinsong Xia^{a*}

^a Wuhan National Laboratory for Optoelectronics, Huazhong University of Science and Technology, Luoyu Road 1037, Wuhan 430074, China

* Email: zengchengwuli@hust.edu.cn and jsxia@hust.edu.cn

† G.C. and C.L. contributed equally to this paper

KEYWORDS. Lithium Niobate, Shortcut to Adiabaticity, Polarization Splitter-Rotator

ABSTRACT: Adiabatic mode evolution waveguides (AMEWs) are widely utilized in integrated photonics, including tapered waveguides, edge couplers, mode converters, splitters, etc. An analytical theory and a novel AMEW design algorithm are developed to create shortcuts to adiabaticity (STA). With the new algorithm, we demonstrate a broadband and highly efficient polarization splitter-rotator (PSR) on a lithium-niobate-on-insulator (LNOI) platform with an LN thickness of 500 nm. The fabricated PSR, with a total length of 2 mm, exhibits an insertion loss (IL) of 0.8 dB and a polarization extinction ratio (ER) of 12 dB over a wavelength range exceeding 76 nm.

INTRODUCTION

Adiabatic mode evolution waveguides (AMEWs) convert power between the guiding modes along the waveguide without mode leakage, if the adiabatic length is sufficient and the propagation constant varies slowly. AMEWs are highly versatile in integrated photonics, offering wide bandwidth (BW) and high robustness, and are used in various applications such as curves¹⁻³, tapers⁴⁻⁶, edge couplers⁷⁻⁹, mode splitters and rotators¹⁰⁻¹², etc. However, most AMEWs are designed with linear tapers, and the lengths of the devices are often definitely large. Linear and segmented-linear AMEWs provide only a few degrees of freedom in the design process¹³, severely restricting their potential for parametric optimization. While existing linear designs are adequate for many applications on the silicon-on-insulator (SOI) platform due to strong light confinement, AMEWs on lower refractive index difference platforms like lithium-niobate-on-insulator (LNOI) tend to be much longer, sometimes excessively long¹⁴ for photonic integrated circuits (PICs). For example, polarization splitter-rotators (PSRs) on 500-nm-thick LNOI platform¹⁴ are considered more challenging compared to 300-nm¹⁵ or 400-nm thickness¹⁶, as the refractive index difference Δn_{eff} at the mode hybridization point is significantly smaller. According to our analysis, there is an inverse square relationship between AMEW length and refractive index difference. Δn_{eff} is very sensitive to the thickness (Δn_{eff} at the hybridization point is about 0.01 on 400-nm-thick LNOI¹⁶ and only about 0.0022 in this work as illustrated in Figure 3b). As observed in various phenomena, e.g. Rabi splitting^{17,18} and dual microring resonators coupling^{19,20}, the difference between the eigenvalues depends

on the coupling strength of the two states. Thinner films are much more conducive to generating strong coupling supermodes for two reasons: (1) Due to the sidewall angle of LNOI waveguides, thinner films allow waveguides to be closer to each other; (2) The mode hybridization point is located in smaller w_1 (0.4 μm on 400-nm-thick LNOI¹⁶ while 0.76 μm on 500-nm-thick LNOI at 1.55 μm wavelength), leading to larger mode overlap. In ref.¹⁴, the total length of the AMEWs on a 500-nm-thick LNOI platform is 7 mm, which is much longer than that on a 400-nm-thick platform¹⁶. Consequently, effective shortcuts to adiabaticity (STA) design algorithms are essential for AMEWs on such low refractive index platforms.

Typically, fully numerical algorithms have been used to design STA for AMEWs^{21,22}, guided by Eigenmode Expansion (EME) simulation results. However, such approaches are time-consuming and demand substantial computing resources. Additionally, the fully numerical algorithms are not impractical for most devices on LNOI due to the overlong lengths (ranging from hundreds of microns to several millimeters), which consume excessive computing memory. Moreover, many numerical algorithms focus on a specific wavelength^{21,23} while bandwidth is increasingly critical in modern PICs. Although there are analytical algorithms for the STA design²⁴⁻²⁶, they often rely on some assumptions to simplify waveguide structures, limiting their applicability. The fast quasi-adiabatic (FAQUAD) algorithm²⁷, an analytical algorithm, has been applied to SOI AMEWs^{4,28}. This algorithm is free of simplification of the waveguide structure and requires only Finite Difference Eigenmode (FDE) simulation for the STA design. However, this algorithm was initially designed for adiabatic quantum computing, so the

reasonability of applying it to AMEWs lacks detailed theoretical analysis. Besides, previous works also focus on a single wavelength, and a broadband design strategy is also highly needed. To address this issue, we first propose the adiabatic waveguide approximation (AWA), which offers a detailed analysis of the mode evolution inside a slowly varying waveguide. Then based on the AWA and the classical FAQUAD, we propose an innovative design algorithm referred to as the broadband FAQUAD to achieve a broad and flexible wavelength range design.

This paper proposes a novel broadband FAQUAD algorithm, providing a bandwidth-flexible design strategy and saving computing resources. To demonstrate the effect of the broadband FAQUAD, we design and fabricate the linear and STA PSRs on 500-nm-thick x-cut LNOI. Simulation results show that the length of the STA PSR is reduced by a factor of 3.5 compared to the linear design. Both simulation and experimental results indicate that the STA PSR exhibits superior performance and a shorter length. The STA PSR achieves an extinct ratio (ER) of 12 dB and an insertion loss (IL) of 0.8 dB over a wide wavelength range from 1.554 μm to beyond 1.63 μm .

THE ADIABATIC WAVEGUIDE APPROXIMATION

The adiabatic quantum approximation (AQA), first demonstrated by M. Born and V. Fock in 1928²⁹, is commonly used in adiabatic quantum computing^{30,31} and annealing³². The AQA states that *a system remains in its instantaneous eigenstate if a given perturbation is acting on it slowly enough*. Although the physics of the Schrödinger and the Helmholtz equations are entirely different, their mathematical nature is similar, because they are both eigenequations (as demonstrated in Table 1). This similarity inspires us to apply the AQA to optics and develop the AWA, starting with the Helmholtz equation without further simplification or assumption on the waveguide structure. The AWA states a similar conclusion to the quantum-mechanical situation: *the electromagnetic wave remains in its instantaneous eigenmode if the perturbation of the waveguide is small enough, i.e. the AMEW length is large enough* (see Supplementary Information).

Table 1. Correspondence with Quantum Mechanics

	QM ^a	WT ^b
Basic Equation	$i\hbar \frac{d}{dt} \Psi\rangle = \hat{H} \Psi\rangle$	$\nabla^2 \Psi + k^2 \Psi = 0$
Longitudinal Direction	t	z
Transverse Direction	x, y, z	x, y
Eigen equation	$\hat{H} n\rangle = E_n n\rangle$	$-(\nabla_t^2 + k^2) \psi_n = -\beta_n^2 \psi_n$
Eigenstate	$ n\rangle$	$\psi_n(x, y)$
Eigenvalue	E_n	$-\beta_n^2$

^a Quantum Mechanics

^b Waveguide Theory

Detailed theoretical analysis (see Supplementary Information) of the AWA indicates that the total length of AMEWs should be long enough to realize the adiabaticity:

$$L \gg C \cdot A_{mn} \quad (1)$$

Where C is a slow-varying term so we consider it as a constant and:

$$A_{mn} = \frac{I_{mn}}{\Delta n_{eff,mn}^2} \frac{dw_1}{d\zeta} \quad (2)$$

With I_{mn} , $\Delta n_{eff,mn}^2$ are the line integration (see Supplementary Information) and the effective index difference between the two modes m and n , and $\zeta = z/L$ is the normalized propagation length.

BASIC STRUCTURE AND THE DESIGN ALGORITHM

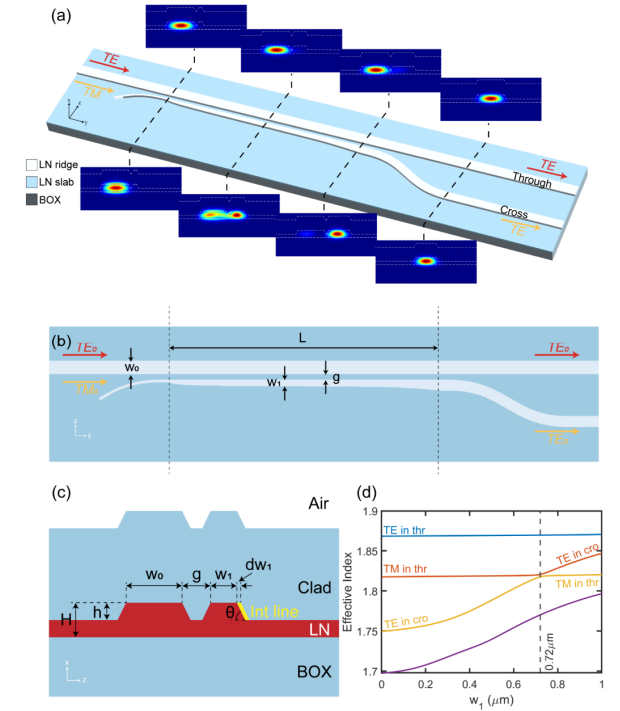


Figure 1. (a) Schematic of the PSR. Top four insets: adiabatic mode evolution process of TE input. The mode remains in through waveguide along the propagation. Bottom four insets: adiabatic mode evolution process of TE input. The mode transferred into the cross waveguide during the propagation. (b) Vertical view of the PSR, with $w_0 = 1.3 \mu\text{m}$, $g = 0.45 \mu\text{m}$, and w_1 varying from $0.3 \mu\text{m}$ to $1 \mu\text{m}$. (c) Waveguide cross-section, with $H = 0.5 \mu\text{m}$, $h = 0.26 \mu\text{m}$ and $\theta = 60^\circ$. Buried oxide (BOX) and clad are both SiO_2 . The integration line is indicated as the yellow line on the right boundary of the cross waveguide (see Supplementary Information). (d) The evolution of the first four modes along the widening w_1 . n_{eff} of TM in through waveguide is larger than TE in drop at first but surpassed when $w_1 > 0.72 \mu\text{m}$, while n_{eff} of TE remains the largest in the entire evolution.

The next paragraph will introduce a detailed description of the broadband FAQUAD algorithm, after a demonstration of the basic structure of the PSR. The schematic (Figure 1a) and vertical view (Figure 1b) illustrate the basic structure of the PSR¹⁶. The waveguides propagate along the y -axis of

the LN crystal. The top width of the through waveguide w_0 is constantly $1.3 \mu\text{m}$, while the cross waveguide top width w_1 widens gradually from $0.3 \mu\text{m}$ to $1 \mu\text{m}$ (top width). The top gap g between the two waveguides is $0.45 \mu\text{m}$. The waveguide cross-section is depicted in Figure 1c, showing a ridge waveguide height (H) of 500 nm and an etch depth (h) of 260 nm . The sidewall angle (θ) is 60° , consistent with our fabrication process. The quasi-transverse-electric mode (TE) in the through waveguide has the largest n_{eff} during the widening of w_1 so the energy stays in the through waveguide. Conversely, the quasi-transverse-magnetic mode (TM) in the through waveguide gradually transfers to TE in the cross waveguide during the process that the n_{eff} of TE in the cross waveguide surpasses that of TM in the through waveguide, as shown in Figure 1d. The mode evolution process is fully illustrated in the insets of Figure 1a.

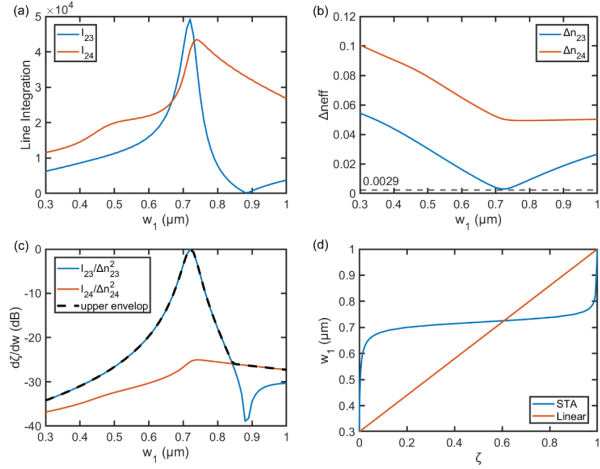


Figure 2. PSR design parameters at a single wavelength of $1.6 \mu\text{m}$. (a) the line integration as a function of w_1 . (b) the refractive index difference as a function of w_1 . The dashed line indicates a minimal value of 0.0029 . (c) Calculated $I_{23}/\Delta n_{23}^2$, $I_{24}/\Delta n_{24}^2$ and their upper envelope as functions of w_1 (d) The line shape of STA compared to linear design.

Based on the basic PSR structure and eq 2, if the AMEW varies linearly (i.e. $dw_1/d\zeta$ is constant), A_{mn} forms a “hill” in the middle of the propagation, as illustrated in Figure 2c. To flatten A_{mn} and shorten the AMEW, we introduce the concept of FAQUAD²⁷:

$$\frac{d\zeta}{dw_1} \propto \frac{I_{mn}}{\Delta n_{eff,mn}^2} \quad (3)$$

So that A_{mn} is invariant during propagation. To ensure the adiabaticity of TM input, we consider $m = 2, n = 3, 4$ in the PSR instance and perform a simulation in FDE. Figure 2a,b illustrate simulated I_{23}, I_{24} and $\Delta n_{eff,23}, \Delta n_{eff,24}$ as functions of w_1 at a wavelength of $1.6 \mu\text{m}$, then c,d are the calculated $I_{23}/\Delta n_{23}^2, I_{24}/\Delta n_{24}^2$ and the STA curve shape. The FAQUAD method only ensures effective conversion in a single wavelength. To design a broadband PSR, a simple way is to select a set of wavelengths in the target range and take their upper envelope, allowing for a flexible design strategy for BW:

$$\frac{d\zeta}{dw_1} = \max \left\{ \frac{I_{2n}^{\lambda_j}}{(\Delta n_{eff,2n}^{\lambda_j})^2} \right\} \quad (4)$$

A set of wavelengths from 1.55 to $1.65 \mu\text{m}$ is used to calculate the broadband PSR, as depicted in Figure 3. This final curve shape is used for fabrication and characterization, and the device length is 2 mm .

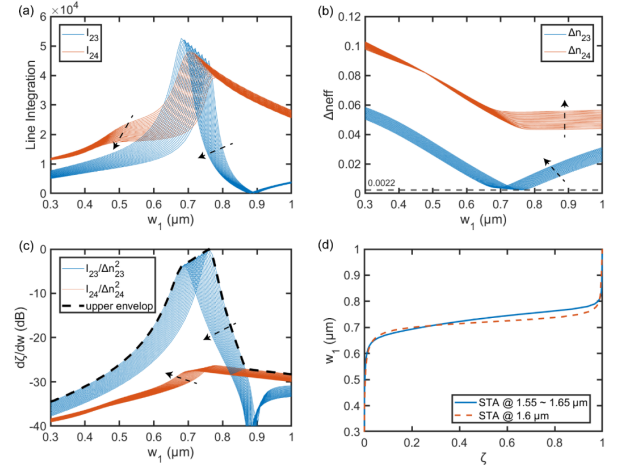


Figure 3. PSR design parameters at a broad wavelength range of $1.55 \sim 1.65 \mu\text{m}$. (a) the line integration as a function of w_1 . (b) the refractive index difference as a function of w_1 . The dashed line indicates a minimal value of 0.0022 . (c) Calculated $I_{23}/\Delta n_{23}^2, I_{24}/\Delta n_{24}^2$ and their upper envelope as functions of w_1 . (d) The line shape of broadband STA compared to single wavelength STA design. All arrows in (a), (b), and (c) indicate the wavelength change from 1.55 to $1.65 \mu\text{m}$.

The linear- and STA-design simulation results of field evolution (Figure 4a), the transmission of TM input to cross port (Figure 4b), and the wavelength sweep of the transmission of TM input to through port (Figure 4c) are presented. The broadband FAQUAD algorithm significantly shortens the PSR by 3.5 times at the $1.6 \mu\text{m}$ wavelength and has a better performance over the target wavelength range compared to the linear design.

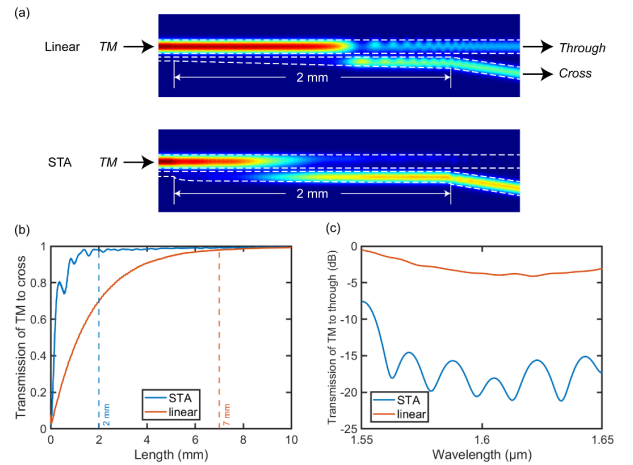


Figure 4. Simulation Results. (a) Field evolution of linear and STA design at $1.6 \mu\text{m}$. The STA design shows a higher conversion efficiency at the same length. (b) Conversion efficiency of STA and linear design when TM input ($1.6 \mu\text{m}$). Vertical lines indicate 98% conversion efficiency to cross port. (c) Bandwidth simulation results of TM input to through port with Linear and STA design at 2 mm length.

DEVICE FABRICATION AND CHARACTERIZATION

To characterize the performance of the broadband FAQUAD, both linear and broadband-STA PSRs are fabricated on a 500-nm-thick x-cut LNOI wafer with a 4.7- μm buried oxide layer (NanoLN), with lengths of 2 mm. The patterns of PSRs on the substrate were achieved using electron beam lithography (EBL) and inductively coupled plasma (ICP) etching, followed by the deposition of a 1- μm -thick SiO_2 layer on the LN via plasma-enhanced chemical vapor deposition (PECVD). Two identical PSRs with different grating couplers are fabricated for TE and TM input, respectively. The microscopy and SEM images of the fabricated PSRs are shown in Figure 5.

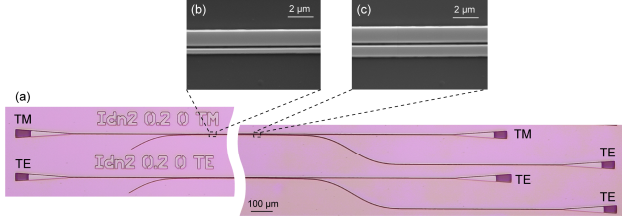


Figure 5. (a) Microscopy image of the STA design PSRs. The GC types for different input polarization are illustrated. (b) SEM image of the start of the AMEW. (c) SEM image of the end of the AMEW.

As depicted in Figure 6a, a tunable laser (TL, Santec TSL-550) is used to generate a continuous-wave (CW) pump ranging from 1.5 to 1.63 μm , then a fiber polarization controller (FPC) is connected to adjust the input polarization. The light coupled out from the chip is collected by a power meter (PM, Santec MPM-210). The experimental results for both linear and STA design are shown in Figure 6, in which b, c for the linear PSR and d, e for the STA design PSR. The insertion loss of the devices is < 0.8 dB within the target wavelength range except for the TM input of linear design, which is due to the low conversion efficiency. The ERs of the TE input are 10.2 dB for the linear PSR and 12.2 dB for the STA design PSR, showing similar performances. However, the linear PSR exhibits an ER of less than 3.4 dB for TM input, corresponding to a conversion efficiency of only $\sim 67\%$. The STA design achieved a large ER of 12.4 dB for TE and TM inputs over a BW exceeding 76 nm, matching the design target and the simulation results well. The test results support the efficiency of the broadband FAQUAD algorithm in shortening AMEWs and enhancing their performances. Besides, we also characterize linear 3-mm and 4-mm linear PSRs, their ERs of TM input are compared in Figure 6f. The linear PSRs have a low ER of less than 7.5 dB in the target

wavelength range. Moreover, the ER exhibits no significant improvement as the length increases, suggesting that the linear PSRs are far from adiabaticity. Additionally, The STA design exhibits a much steeper BW cutoff of around 1.55 μm compared to the linear design, indicating that the shortening of the AMEW comes from sacrificing the device performance in the unwanted wavelength range.

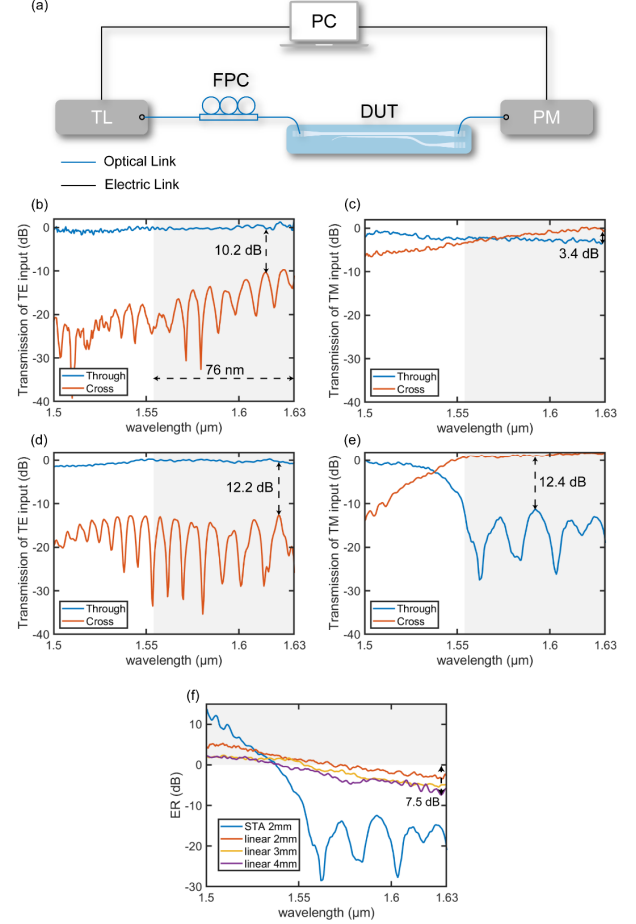


Figure 6. (a) Test configuration. TL: Tunable Laser. FPC: Fiber Polarization Controller. DUT: Device Under Test. PM: Power Meter. PC: Personal Computer. And test results of (b) TE and (c) TM input of linear PSR. (d) TE and (e) TM input of STA PSR. The results show a 12 dB ER with an over 76-nm BW (1.554 \sim 1.63 μm corresponds to the area). (f) ER comparison of STA and linear PSR when TM input. The ER is calculated by $T_{thr}(\text{dB}) - T_{cro}(\text{dB})$. The positive values in the shaded area are because the conversion efficiency is less than 50%.

Table 2. Performances of several PSRs on LNOI

Ref.	Shape	LN thickness/nm	L/ mm	ER/dB	IL/ dB	BW/nm
15	Segmented-linear & MMI	360	0.6	10	1.5	47
16	Linear	400	1	20	0.5	110
14	Segmented-linear	500	7	10	3	130
35	Segmented-linear & Y-junction	500	0.44	19.6	1	60
33	Segmented-linear & ADC	600	0.24	10.6	0.91	50
34	MMI	600	1.6	9.5	3	39
This work	STA	500	2	12.2	0.8	76

Table 2 illustrates the comparison of several PSRs. Some PSRs exhibit large ERs, BWs, and short lengths because they are fabricated on a thinner LNOI platform¹⁶ or propagate along the z-axis³³, having a larger Δn_{eff} at the mode hybridization point than our PSR thus being easier for PSR applications. The MMI^{15,34}, Y-junction³⁵, and ADC³³ approaches provide shorter device lengths but limited BW. Our STA PSR shows a balanced length, ER, BW, and IL performance.

DISCUSSION AND CONCLUSION

This work builds a bridge between the AWA and the AQA³⁶. Developed for decades, more accurate theoretical approximations, estimations³⁷, and advanced algorithms³⁸ used in AQA are also available for designing STA AMEWs, promising more strategies to enhance their performances further.

In conclusion, a novel design strategy is developed for designing AMEWs, providing significant length reduction and flexible BW selection. We then fabricate and test a PSR using this strategy, and both simulation and test results have demonstrated the effectiveness of the broadband FAQUAD in reducing the total length of AMEWs while maintaining the desired BW. A total BW of over 76 nm with a 12 dB ER is achieved with a length of only 2 mm.

ASSOCIATED CONTENT

The Supporting Information is available free of charge via the Internet at <http://pubs.acs.org>.

Detail Analysis of the Adiabatic Waveguide Approximation and the adiabaticity condition.

AUTHOR INFORMATION

Corresponding Authors

Jinsong Xia - Wuhan National Laboratory for Optoelectronics, Huazhong University of Science and Technology, Wuhan 430074, China; Email: jsxia@hust.edu.cn.

Cheng Zeng - Wuhan National Laboratory for Optoelectronics, Huazhong University of Science and Technology, Wuhan 430074, China; Email: zengchengwuli@hust.edu.cn.

Authors

Geng Chen - Wuhan National Laboratory for Optoelectronics, Huazhong University of Science and Technology, Wuhan 430074, China; orcid.org/0009-0003-6891-2225

Chijun Li - Wuhan National Laboratory for Optoelectronics, Huazhong University of Science and Technology, Luoyu Road 1037, Wuhan 430074, China

Xuanhao Wang - Wuhan National Laboratory for Optoelectronics, Huazhong University of Science and Technology, Luoyu Road 1037, Wuhan 430074, China

Yuankang Huang - Wuhan National Laboratory for Optoelectronics, Huazhong University of Science and Technology, Luoyu Road 1037, Wuhan 430074, China

Siyu Lu - Wuhan National Laboratory for Optoelectronics, Huazhong University of Science and Technology, Luoyu Road 1037, Wuhan 430074, China

Yiqi Dai - Wuhan National Laboratory for Optoelectronics, Huazhong University of Science and Technology, Luoyu Road 1037, Wuhan 430074, China

Xiangyu Meng - Wuhan National Laboratory for Optoelectronics, Huazhong University of Science and Technology, Luoyu Road 1037, Wuhan 430074, China

Author Contributions

G.C. and C.L. conceived the experiment. G.C. and X.W. designed the devices. G.C. and C.L. fabricated the devices. G.C. performed theoretical analysis and numerical simulations of the PSRs. G.C., Y.H., and S.L. carried out the device characterization. G.C., Y.D., and X.M. performed the data analysis. G.C. wrote the manuscript with contributions from all authors. C.Z. and J.X. supervised the project.

Funding Sources

This work is supported by National Key Research and Development Program of China (2022YFB2802402), and the National Natural Science Foundation of China under Grant No. 62175079, 62205119, and the Natural Science Foundation of Hubei Province under Grant No. 2020CFA004.

ACKNOWLEDGMENT

We acknowledge support for nanofabrication from the cleanroom of HUST.

REFERENCE

- (1) Chen, T.; Lee, H.; Li, J.; Vahala, K. J. A General Design Algorithm for Low Optical Loss Adiabatic Connections in Waveguides. *Opt. Express* **2012**, *20* (20), 22819–22829. <https://doi.org/10.1364/OE.20.022819>.
- (2) Cherchi, M.; Ylinen, S.; Harjanne, M.; Kapulainen, M.; Aalto, T. Dramatic Size Reduction of Waveguide Bends on a Micron-Scale Silicon Photonic Platform. *Opt. Express* **2013**, *21* (15), 17814–17823. <https://doi.org/10.1364/OE.21.017814>.
- (3) Jiang, X.; Wu, H.; Dai, D. Low-Loss and Low-Crosstalk Multimode Waveguide Bend on Silicon. *Opt. Express* **2018**, *26* (13), 17680–17689. <https://doi.org/10.1364/OE.26.017680>.
- (4) Chung, H.-C.; Tseng, S.-Y. Ultrashort and Broadband Silicon Polarization Splitter-Rotator Using Fast Quasiadiabatic Dynamics. *Opt. Express* **2018**, *26* (8), 9655–9665. <https://doi.org/10.1364/OE.26.009655>.
- (5) Liu, Y.; Sun, W.; Xie, H.; Zhang, N.; Xu, K.; Yao, Y.; Xiao, S.; Song, Q. Adiabatic and Ultracompact Waveguide Tapers Based on Digital Metamaterials. *IEEE J. Sel. Top. Quantum Electron.* **2019**, *25* (3), 1–6. <https://doi.org/10.1109/JSTQE.2018.2846046>.
- (6) Karim, M. R.; Al Kayed, N.; Rafi, R.; Rahman, B. M. A. Design and Analysis of Inverse Tapered Silicon Nitride Waveguide for Flat and Highly Coherent Supercontinuum Generation in the Mid-Infrared. *Opt. Quantum Electron.* **2023**, *56* (1), 68. <https://doi.org/10.1007/s11082-023-05636-5>.
- (7) Krasnokutskaya, I.; Tambasco, J.-L. J.; Peruzzo, A. Nanostructuring of LNOI for Efficient Edge Coupling. *Opt. Express* **2019**, *27* (12), 16578–16585. <https://doi.org/10.1364/OE.27.016578>.
- (8) He, A.; Guo, X.; Wang, K.; Zhang, Y.; Su, Y. Low Loss, Large Bandwidth Fiber-Chip Edge Couplers Based on Silicon-on-Insulator Platform. *J. Light. Technol.* **2020**, *38* (17), 4780–4786.
- (9) Bhandari, B.; Im, C.-S.; Lee, K.-P.; Kim, S.-M.; Oh, M.-C.; Lee, S.-S. Compact and Broadband Edge Coupler Based on Multi-Stage Silicon Nitride Tapers. *IEEE Photonics J.* **2020**, *12* (6), 1–11. <https://doi.org/10.1109/JPHOT.2020.3036498>.
- (10) Sacher, W. D.; Barwicz, T.; Taylor, B. J. F.; Poon, J. K. S. Polarization Rotator-Splitters in Standard Active Silicon Photonics Platforms. *Opt. Express* **2014**, *22* (4), 3777–3786. <https://doi.org/10.1364/OE.22.003777>.
- (11) Wang, J.; Niu, B.; Sheng, Z.; Wu, A.; Li, W.; Wang, X.; Zou, S.; Qi, M.; Gan, F. Novel Ultra-Broadband Polarization Splitter-Rotator Based on Mode-Evolution Tapers and a Mode-Sorting Asymmetric Y-Junction. *Opt. Express* **2014**, *22* (11), 13565–

13571. <https://doi.org/10.1364/OE.22.013565>.
- (12) Chung, H.-P.; Lee, C.-H.; Huang, K.-H.; Yang, S.-L.; Wang, K.; Solntsev, A. S.; Sukhorukov, A. A.; Setzpfandt, F.; Chen, Y.-H. Broadband On-Chip Polarization Mode Splitters in Lithium Niobate Integrated Adiabatic Couplers. *Opt. Express* **2019**, *27* (2), 1632–1645. <https://doi.org/10.1364/OE.27.001632>.
- (13) Luo, H.; Chen, Z.; Li, H.; Chen, L.; Han, Y.; Lin, Z.; Yu, S.; Cai, X. High-Performance Polarization Splitter-Rotator Based on Lithium Niobate-on-Insulator Platform. *IEEE Photonics Technol. Lett.* **2021**, *33* (24), 1423–1426. <https://doi.org/10.1109/LPT.2021.3123101>.
- (14) Chen, Z.; Yang, J.; Wong, W.-H.; Pun, E. Y.-B.; Wang, C. Broadband Adiabatic Polarization Rotator-Splitter Based on a Lithium Niobate on Insulator Platform. *Photonics Res.* **2021**, *9* (12), 2319–2324. <https://doi.org/10.1364/PRJ.432906>.
- (15) Deng, C.; Zhu, W.; Sun, Y.; Lu, M.; Huang, L.; Wang, D.; Hu, G.; Yun, B.; Cui, Y. Broadband Polarization Splitter-Rotator on Lithium Niobate-on-Insulator Platform. *IEEE Photonics Technol. Lett.* **2023**, *35* (1), 7–10. <https://doi.org/10.1109/LPT.2022.3215268>.
- (16) Gan, R.; Qi, L.; Ruan, Z.; Liu, J.; Guo, C.; Chen, K.; Liu, L. Fabrication Tolerant and Broadband Polarization Splitter-Rotator Based on Adiabatic Mode Evolution on Thin-Film Lithium Niobate. *Opt. Lett.* **2022**, *47* (19), 5200–5203. <https://doi.org/10.1364/OL.470216>.
- (17) Yoshie, T.; Scherer, A.; Hendrickson, J.; Khitrova, G.; Gibbs, H. M.; Rupper, G.; Ell, C.; Shchekin, O. B.; Deppe, D. G. Vacuum Rabi Splitting with a Single Quantum Dot in a Photonic Crystal Nanocavity. *Nature* **2004**, *432* (7014), 200–203. <https://doi.org/10.1038/nature03119>.
- (18) Toida, H.; Nakajima, T.; Komiyama, S. Vacuum Rabi Splitting in a Semiconductor Circuit QED System. *Phys. Rev. Lett.* **2013**, *110* (6), 066802. <https://doi.org/10.1103/PhysRevLett.110.066802>.
- (19) Zhang, M.; Wang, C.; Hu, Y.; Shams-Ansari, A.; Ren, T.; Fan, S.; Lončar, M. Electronically Programmable Photonic Molecule. *Nat. Photonics* **2019**, *13* (1), 36–40. <https://doi.org/10.1038/s41566-018-0317-y>.
- (20) Tikan, A.; Riemensberger, J.; Komagata, K.; Hönl, S.; Churaev, M.; Skehan, C.; Guo, H.; Wang, R. N.; Liu, J.; Seidler, P.; Kippenberg, T. J. Emergent Nonlinear Phenomena in a Driven Dissipative Photonic Dimer. *Nat. Phys.* **2021**, *17* (5), 604–610. <https://doi.org/10.1038/s41567-020-01159-y>.
- (21) Liang, T.-L.; Tu, Y.; Chen, X.; Huang, Y.; Bai, Q.; Zhao, Y.; Zhang, J.; Yuan, Y.; Li, J.; Yi, F.; Shao, W.; Ho, S.-T. A Fully Numerical Method for Designing Efficient Adiabatic Mode Evolution Structures (Adiabatic Taper, Coupler, Splitter, Mode Converter) Applicable to Complex Geometries. *J. Light. Technol.* **2021**, *39* (17), 5531–5547. <https://doi.org/10.1109/JLT.2021.3085306>.
- (22) Liang, T.-L.; Cheng, X.; Shi, J.; Wu, G.; Xu, K.; Rong, W.; Lin, L.; Shao, W. Analysis and Design of Compact Adiabatic Mode Converters Based on Adiabatic Mode Evolutions. *J. Light. Technol.* **2023**, *41* (19), 6356–6361. <https://doi.org/10.1109/JLT.2023.3278679>.
- (23) Liang, T.; Cheng, X.; Yu, M.; Zhang, L.; Shi, J.; Shao, W. Numerical Method for Designing Ultrashort and Efficient Adiabatic Mode Converters. *JOSA B* **2022**, *39* (10), 2637–2642. <https://doi.org/10.1364/JOSAB.468543>.
- (24) Milton, A.; Burns, W. Mode Coupling in Optical Waveguide Horns. *IEEE J. Quantum Electron.* **1977**, *13* (10), 828–835. <https://doi.org/10.1109/JQE.1977.1069240>.
- (25) Ramadan, T. A.; Scarmozzino, R.; Osgood, R. M. Adiabatic Couplers: Design Rules and Optimization. *J. Light. Technol.* **1998**, *16* (2), 277–283. <https://doi.org/10.1109/50.661021>.
- (26) Sun, X.; Liu, H.-C.; Yarif, A. Adiabaticity Criterion and the Shortest Adiabatic Mode Transformer in a Coupled-Waveguide System. *Opt. Lett.* **2009**, *34* (3), 280–282. <https://doi.org/10.1364/OL.34.000280>.
- (27) Martínez-Garaot, S.; Ruschhaupt, A.; Gillet, J.; Busch, Th.; Muga, J. G. Fast Quasiadiabatic Dynamics. *Phys. Rev. A* **2015**, *92* (4), 043406. <https://doi.org/10.1103/PhysRevA.92.043406>.
- (28) Chen, C.-H.; Lo, Y.-F.; Lu, G.-X.; Hung, Y.-J.; Tseng, S.-Y. Adiabaticity Engineered Silicon Coupler With Design-Intended Splitting Ratio. *IEEE Photonics J.* **2024**, *16* (2), 1–5. <https://doi.org/10.1109/JPHOT.2024.3383439>.
- (29) Born, M.; Fock, V. Beweis des Adiabatenatzes. *Z. Für Phys.* **1928**, *51* (3), 165–180. <https://doi.org/10.1007/BF01343193>.
- (30) Barends, R.; Shabani, A.; Lamata, L.; Kelly, J.; Mezzacapo, A.; Heras, U. L.; Babbush, R.; Fowler, A. G.; Campbell, B.; Chen, Y.; Chen, Z.; Chiaro, B.; Dunsworth, A.; Jeffrey, E.; Lucero, E.; Megrant, A.; Mutus, J. Y.; Neeley, M.; Neill, C.; O'Malley, P. J. J.; Quintana, C.; Roushan, P.; Sank, D.; Vainsencher, A.; Wenner, J.; White, T. C.; Solano, E.; Neven, H.; Martinis, J. M. Digitized Adiabatic Quantum Computing with a Superconducting Circuit. *Nature* **2016**, *534* (7606), 222–226. <https://doi.org/10.1038/nature17658>.
- (31) Hegade, N. N.; Paul, K.; Ding, Y.; Sanz, M.; Albarrán-Arriagada, F.; Solano, E.; Chen, X. Shortcuts to Adiabaticity in Digitized Adiabatic Quantum Computing. *Phys. Rev. Appl.* **2021**, *15* (2), 024038. <https://doi.org/10.1103/PhysRevApplied.15.024038>.
- (32) Mandrà, S.; Zhu, Z.; Katzgraber, H. G. Exponentially Biased Ground-State Sampling of Quantum Annealing Machines with Transverse-Field Driving Hamiltonians. *Phys. Rev. Lett.* **2017**, *118* (7), 070502. <https://doi.org/10.1103/PhysRevLett.118.070502>.
- (33) Wu, Y.; Sun, X.; Xue, X.; Li, H.; Liu, S.; Zheng, Y.; Chen, X. Compact Adiabatic Polarization Splitter-Rotator on Thin-Film Lithium Niobate. *J. Light. Technol.* **2024**, *42* (7), 2429–2435. <https://doi.org/10.1109/JLT.2023.3338229>.
- (34) Wang, M.; Yao, H.; Deng, J.; Hu, Z.; Tang, T.; Chen, K. Polarization Splitter Rotator on Thin Film Lithium Niobate Based on Multimode Interference. *arXiv February 23, 2024*. <https://doi.org/10.48550/arXiv.2402.15203>.
- (35) Wang, X.; Pan, A.; Li, T.; Zeng, C.; Xia, J. Efficient Polarization Splitter-Rotator on Thin-Film Lithium Niobate. *Opt. Express* **2021**, *29* (23), 38044–38052. <https://doi.org/10.1364/OE.443798>.
- (36) Amin, M. H. S. Consistency of the Adiabatic Theorem. *Phys. Rev. Lett.* **2009**, *102* (22), 220401. <https://doi.org/10.1103/PhysRevLett.102.220401>.
- (37) Venuti, L. C.; Albash, T.; Lidar, D. A.; Zanardi, P. Adiabaticity in Open Quantum Systems. *Phys. Rev. A* **2016**, *93* (3), 032118. <https://doi.org/10.1103/PhysRevA.93.032118>.
- (38) Albash, T.; Lidar, D. A. Adiabatic Quantum Computation. *Rev. Mod. Phys.* **2018**, *90* (1), 015002. <https://doi.org/10.1103/RevModPhys.90.015002>.

Supplementary Information

Corresponding to Quantum Mechanics

In waveguides, we consider the Helmholtz equation as the start:

$$\nabla^2 \Psi(x, y, z) + k^2 \Psi(x, y, z) = 0 \quad (S1)$$

Where ∇ is the nabla operator, Ψ is the electric or magnetic field, and $k = 2\pi n/\lambda$ is the wavenumber. To solve eigenmodes of waveguide in a certain propagation distance z , divide Ψ as $\Psi(x, y, z) = \psi(x, y)Z(z)$, then:

$$(\nabla_t^2 + k^2)\psi = \beta^2 \psi \quad (S2)$$

Where β is the propagation constant and $\nabla_t^2 = \nabla^2 - d^2/dz^2$ is the transverse nabla operator. Rewriting eqs S1, S2 in the form of Hamiltonian and Dirac notation:

$$\frac{d^2}{dz^2} |\Psi(z)\rangle = \hat{H} |\Psi(z)\rangle \quad (S3)$$

$$\hat{H}(z) |n(z)\rangle = -\beta_n^2 |n(z)\rangle \quad (S4)$$

Where $\hat{H}(z) = -(\nabla_t^2 + k^2)$, $|\Psi(z)\rangle = \Psi(x, y, z)$, $|n(z)\rangle$ and $\beta_n(z)$ represent the n -th eigenmode and propagation constant in the distance z . Normalize eqs S3, S4 with $\zeta = z/L$, where L is the total length of the structure:

$$\frac{d^2}{d\zeta^2} |\tilde{\Psi}(\zeta)\rangle = L^2 \tilde{H}(\zeta) |\tilde{\Psi}(\zeta)\rangle \quad (S5)$$

$$\tilde{H}(\zeta) |\tilde{n}(\zeta)\rangle = -\tilde{\beta}_n^2(\zeta) |\tilde{n}(\zeta)\rangle \quad (S6)$$

The tilde will be omitted in the following analysis for simplicity. Define the inner product as:

$$\langle \psi | \varphi \rangle = \iint_S (\mathbf{E}_\psi \times \mathbf{H}_\varphi^* + \mathbf{E}_\varphi^* \times \mathbf{H}_\psi) ds \quad (S7)$$

In which \mathbf{E} , \mathbf{H} are normalized field components and then the orthogonality of different modes $\langle m | n \rangle = \delta_{mn}$ is satisfied. Here we introduce two crucial lemmas [21,39]:

$$\langle m | \frac{d}{d\zeta} |n\rangle = \frac{1}{\beta_m^2 - \beta_n^2} \langle m | \frac{dH}{d\zeta} |n\rangle \quad (S8)$$

$$\text{Re} \left\langle \left\langle m | \frac{d}{d\zeta} |m\rangle \right\rangle \right\rangle = 0 \quad (S9)$$

Lightwave Propagation

Assume that the start state is:

$$|\Psi(0)\rangle = \sum_n c_n(0) e^{-i\theta_n(0)} |n(0)\rangle \quad (S10)$$

Where $c_n(\zeta)$ is the mode expansion coefficient of the n -th eigenmode at ζ and $|c_n(\zeta)|^2$ represents the energy in the mode; θ_n is the phase cumulated during the propagation of the n -th mode and $d\theta_n/dz$, so:

$$\frac{d}{d\zeta} \theta_n(\zeta) = L\beta_n(\zeta) \quad (S11)$$

Substituting eq S5 into eq S10:

$$\begin{aligned}
\text{LHS} &= \sum_n \frac{d^2}{d\zeta^2} (c_n e^{-i\theta_n} |n\rangle) \\
&= \sum_n \left(\frac{d^2 c_n}{d\zeta^2} e^{-i\theta_n} |n\rangle - L^2 \beta_n^2 c_n e^{-i\theta_n} |n\rangle + c_n e^{-i\theta_n} \frac{d^2 |n\rangle}{d\zeta^2} \right. \\
&\quad \left. - 2iL\beta_n \frac{dc_n}{d\zeta} e^{-i\theta_n} |n\rangle + 2 \frac{dc_n}{d\zeta} e^{-i\theta_n} \frac{d|n\rangle}{d\zeta} - 2iL\beta_n c_n e^{-i\theta_n} \frac{d|n\rangle}{d\zeta} \right) \\
\text{RHS} &= \sum_n H(c_n e^{-i\theta_n} |n\rangle) = \sum_n c_n e^{-i\theta_n} H|n\rangle = \sum_n -L^2 \beta_n^2 c_n e^{-i\theta_n} |n\rangle
\end{aligned} \tag{S12}$$

Note that RHS equals to second term of LHS, and take the inner product with $|m\rangle$:

$$\begin{aligned}
& -\frac{1}{L} \frac{d^2 c_m}{d\zeta^2} + 2i\beta_m \frac{dc_m}{d\zeta} - 2 \left(\frac{1}{L} \frac{dc_m}{d\zeta} - i\beta_m c_m \right) \langle m | \frac{d}{d\zeta} |m\rangle \\
& = \sum_{n \neq m} e^{i(\theta_m - \theta_n)} \left[\left(\frac{2}{L} \frac{dc_n}{d\zeta} - i\beta_n c_n \right) \langle m | \frac{d}{d\zeta} |n\rangle + \frac{c_n}{L} \langle m | \frac{d^2}{d\zeta^2} |n\rangle \right]
\end{aligned} \tag{S13}$$

Here we apply two approximations. Firstly, as $L \rightarrow \infty$, all terms with L on the denominators are neglectable:

$$\frac{1}{c_m} \frac{dc_m}{d\zeta} + \langle m | m \rangle = \sum_{n \neq m} -\frac{\beta_n / \beta_m}{2(\beta_m^2 - \beta_n^2)} \frac{c_n}{c_m} e^{i(\theta_m - \theta_n)} \langle m | \frac{dH}{d\zeta} |n\rangle \tag{S14}$$

In which we use eq S8. Integrate S14, we get:

$$\ln c_m \Big|_0^\zeta + \int_0^\zeta d\zeta_1 \langle m | \frac{d}{d\zeta_1} |m\rangle = -\sum_{n \neq m} \int_0^\zeta d\zeta_1 \frac{\beta_n / \beta_m}{2(\beta_m^2 - \beta_n^2)} \frac{c_n}{c_m} e^{i(\theta_m - \theta_n)} \langle m | \frac{dH}{d\zeta_1} |n\rangle \tag{S15}$$

Then we take the second approximation. For any $f(\zeta)$:

$$\begin{aligned}
\int_0^\zeta d\zeta_1 f(\zeta_1) e^{i(\theta_m - \theta_n)} &= \frac{1}{iL} \int_0^\zeta \frac{f(\zeta_1)}{\beta_m - \beta_n} d e^{i(\theta_m - \theta_n)} \\
&= \frac{f(\zeta_1) e^{i(\theta_m - \theta_n)} \Big|_0^\zeta}{iL(\beta_m - \beta_n)} + \frac{1}{iL} \int_0^\zeta e^{i(\theta_m - \theta_n)} d \frac{f(\zeta_1)}{(\beta_m - \beta_n)} \\
&= o(1/L) + \frac{1}{iL} \int_0^\zeta d\zeta_1 e^{i(\theta_m - \theta_n)} \frac{f'(\zeta_1)(\beta_m - \beta_n) - f(\zeta_1)(\beta_m' - \beta_n')}{(\beta_m - \beta_n)^2} \\
&= o(1/L) + o(1/L^2) + \dots
\end{aligned} \tag{S16}$$

So, the eq S15 RHS = $o(1/L)$ and the final expression about c_m becomes:

$$\ln c_m \Big|_0^\zeta = i \int_0^\zeta d\zeta_1 i \langle m | \frac{d}{d\zeta_1} |m\rangle \tag{S17}$$

$$c_m(\zeta) = c_m(0) e^{\int_0^\zeta d\zeta_1 i \langle m | \frac{d}{d\zeta_1} |m\rangle} = c_m(0) e^{i\gamma(\zeta)} \tag{S18}$$

Thus, we get a conclusion the same as AQA with $\gamma(\zeta)$ corresponding to the Berry Phase [39]. Obviously, $|c_m|^2$ is a constant, and this means that the power in each eigenmode won't exchange with the others', which is so-called "adiabaticity".

Approximation Analysis

Consider the terms that have been eliminated in the second approximation and integrate them by parts:

$$\begin{aligned}
& \int_0^\zeta d\zeta_1 \frac{\beta_n / \beta_m}{2(\beta_m^2 - \beta_n^2)} \frac{c_n}{c_m} e^{i(\theta_m - \theta_n)} \langle m | \frac{dH}{d\zeta_1} |n\rangle \\
&= \int_0^\zeta \frac{\beta_n / \beta_m}{iL(\beta_m^2 - \beta_n^2)(\beta_m - \beta_n)} \frac{c_n}{c_m} \langle m | \frac{dH}{d\zeta_1} |n\rangle d e^{i(\theta_m - \theta_n)} \\
&= \frac{e^{i(\theta_m - \theta_n)} \beta_n / \beta_m}{iL(\beta_m^2 - \beta_n^2)(\beta_m - \beta_n)} \frac{c_n}{c_m} \langle m | \frac{dH}{d\zeta_1} |n\rangle \Big|_0^\zeta + o(1/L^2)
\end{aligned} \tag{S19}$$

So, the condition of adiabatic transform is written as:

$$L \gg \left| \frac{e^{i(\theta_m - \theta_n)} \beta_n / \beta_m}{(\beta_m^2 - \beta_n^2)(\beta_m - \beta_n)} \langle m | \frac{dH}{d\zeta} |n\rangle \right| = \frac{\beta_n / \beta_m}{(\beta_m^2 - \beta_n^2)(\beta_m - \beta_n)} \left| \langle m | \frac{dH}{d\zeta} |n\rangle \right| \tag{S20}$$

Where c_n/c_m is not included in the condition as its module is constant and does not impact our algorithm. Substitute $|m\rangle, |n\rangle$ and \hat{H} in the eq S20:

$$\begin{aligned} \text{RHS} &= \frac{\beta_n/\beta_m}{(\beta_m^2 - \beta_n^2)(\beta_m - \beta_n)} \left| \iint_S ds \left(\mathbf{E}_m \times \frac{d\mathbf{k}^2}{d\zeta} \mathbf{H}_n^* + \frac{d\mathbf{k}^2}{d\zeta} \mathbf{E}_n^* \times \mathbf{H}_m \right) \right| \\ &= \frac{\lambda}{2\pi} \frac{n_{\text{eff},n}/n_{\text{eff},m}}{(n_{\text{eff},m} + n_{\text{eff},n})(n_{\text{eff},m} - n_{\text{eff},n})} \left| \iint_S ds \left(\mathbf{E}_m \times \frac{d\mathbf{k}^2}{d\zeta} \mathbf{H}_n^* + \frac{d\mathbf{k}^2}{d\zeta} \mathbf{E}_n^* \times \mathbf{H}_m \right) \right| \end{aligned} \quad (\text{S21})$$

Using $\mathbf{k}^2 = \omega^2 \boldsymbol{\epsilon} \boldsymbol{\mu} = (2\pi/\lambda)^2 \boldsymbol{\epsilon}_r$, we get the adiabaticity condition as:

$$L \gg C \frac{\left| \iint_S ds \left(\mathbf{E}_m \times \frac{d\boldsymbol{\epsilon}_r}{d\zeta} \mathbf{H}_n^* + \frac{d\boldsymbol{\epsilon}_r}{d\zeta} \mathbf{E}_n^* \times \mathbf{H}_m \right) \right|}{\Delta n_{\text{eff},mn}^2} \quad (\text{S22})$$

Where:

$$C = \frac{\lambda}{2\pi} \frac{n_{\text{eff},n}/n_{\text{eff},m}}{n_{\text{eff},m} + n_{\text{eff},n}}, \Delta n_{\text{eff},mn} = n_{\text{eff},m} - n_{\text{eff},n} \quad (\text{S23})$$

C usually changes very slowly, so the parts of the integration and the $\Delta n_{\text{eff},mn}$ matter more in the design of STA. Next, we will demonstrate the design strategy with the example of the PSR.

After defining the basic structure (see Basic Structure and the STA Design), the integration in the eq S22 could be further simplified:

$$\text{Int} = \left| \iint_S ds \left(\mathbf{E}_m \times \frac{d\boldsymbol{\epsilon}_r}{dw_1} \mathbf{H}_n^* + \frac{d\boldsymbol{\epsilon}_r}{dw_1} \mathbf{E}_n^* \times \mathbf{H}_m \right) \right| \frac{dw_1}{d\zeta} \quad (\text{S24})$$

Where $d\boldsymbol{\epsilon}_r/dw_1$ can be expressed as:

$$\frac{d\boldsymbol{\epsilon}_r}{dw_1} = \Delta \boldsymbol{\epsilon}_r \frac{\delta[(x, y) \in (l \times dw_1)]}{dw_1} \quad (\text{S25})$$

Where $\Delta \boldsymbol{\epsilon}_r = \boldsymbol{\epsilon}_r(\text{core}) - \boldsymbol{\epsilon}_r(\text{clad})$, and $(l \times dw_1)$ represents the quadrangular area defined by the integration line and dw_1 shown in Figure 1c and δ is the Dirac function. Eq S25 indicates an abrupt change of permittivity in the quadrangle, and the fact that dw_1 is a differentiation symbol degenerates the surface integration into a line integration as:

$$\text{Int} = \sin \theta \left| \int_l \left(\mathbf{E}_m \times \Delta \boldsymbol{\epsilon}_r \mathbf{H}_n^* + \Delta \boldsymbol{\epsilon}_r \mathbf{E}_n^* \times \mathbf{H}_m \right) \mathbf{z} ds \right| \frac{dw_1}{d\zeta} \quad (\text{S26})$$

Where θ is the sidewall angle of the waveguides and \mathbf{z} is the unit vector of propagation direction. Define:

$$A_{mn} \equiv \frac{\left| \int_l \left(\mathbf{E}_m \times \Delta \boldsymbol{\epsilon}_r \mathbf{H}_n^* + \Delta \boldsymbol{\epsilon}_r \mathbf{E}_n^* \times \mathbf{H}_m \right) \mathbf{z} dl \right|}{\Delta n_{\text{eff},mn}^2} \frac{dw_1}{d\zeta} = \frac{I}{\Delta n_{\text{eff},mn}^2} \frac{dw_1}{d\zeta} \quad (\text{S27})$$

Putting $\sin \theta$ into C , the adiabaticity condition could be concisely expressed as:

$$L \gg C \cdot A_{mn} \quad (\text{S28})$$